Karim Fendi, Nedjima Bouzidi, Reguia Boudraa, Amira Saidani, Amar Manseri, Dolores Eliche Quesada, Tran Nguyen Hai, Jean-Claude Bollinger, Stefano Salvestrini, Mohamed Kebir, Nacer Belkessa and Lotfi Mouni*

Testing of kaolinite/TiO_2 nanocomposites for methylene blue removal: photodegradation and mechanism

https://doi.org/10.1515/ijcre-2024-0145
Received July 20, 2024; accepted December 20, 2024; published online January 6, 2025

Abstract: This study investigated the effect of different treatment conditions on kaolinite-halloysite type as a support for TiO_2 and their potential application in photocatalysis. These nanocomposites are used to study the photodegradation of methylene blue, a dye widely used in the textile industry and released into the environment. Crystal structure, specific surface area, pore structure and the morphology of kaolinite were all studied using XRD, attenuated total reflectance (ATR), Brunauer-Emmett-Teller (BET), scanning electron microscopy (SEM) and ultraviolet-visible light. The optical band gap increased with increasing kaolin loading from 2.93 to 3.14 eV. Compared with pure TiO_2 photocatalyst, the morphology and structure of kaolinite/TiO_2 composites can significantly improve their ability to adsorb organic pollutants and their photocatalytic activity: The photocatalytic efficiency of kaolinite/TiO_2 was evaluated by degrading the textile dye methylene blue (MB) under UV-light irradiation. The results showed an improvement from 71 % using TiO_2 to 98 % for nanocomposites kaolinite/TiO_2 using samples amount of 1 g/L and Co = 20 mg/L.

Keywords: kaolinite; TiO_2; adsorption; photodegradation; methylene blue; nanocomposites

***Corresponding author: Lotfi Mouni**, Laboratoire de Gestion et Valorisation des Ressources Naturelles et Assurance Qualité, Faculté SNVST, Université de Bouira, Bouira 10000, Algeria, E-mail: l.mouni@univ-bouira.dz. https://orcid.org/0000-0002-5259-2357
Karim Fendi and Amira Saidani, Laboratory Processes for Materials, Energy, Water and Environment, Faculty of Science and Technology, University of Bouira, 10000 Bouira, Algeria
Nedjima Bouzidi, Laboratoire de Technologie des matériaux et du génie des procédés (LTMGP), Faculté de Technologie, Université de Bejaia, 06000 Bejaia, Algeria
Reguia Boudraa, Laboratory of Materials and Durable Development (LM2D), University of Bouira, 10000 Bouira, Algeria
Amar Manseri, Research Center of Semi-Conductor Technology for Energy, CRTSE – 02, Bd. Dr. Frantz Fanon, B.P. 140, 7 Merveilles 16038 Algiers, Algeria
Dolores Eliche Quesada, Department of Chemical, Environmental, and Materials Engineering, Higher Polytechnic School of Jaén, University of Jaén, Campus Las Lagunillas s/n, 23071 Jaén, Spain
Tran Nguyen Hai, Center for Energy and Environmental Materials, Institute of Fundamental and Applied Sciences, Duy Tan University, Ho Chi Minh, 700000, Vietnam; and Faculty of Environmental and Chemical Engineering, Duy Tan University, Da Nang, 550000, Vietnam. https://orcid.org/0000-0001-8361-2616
Jean-Claude Bollinger, Laboratoire E2Lim (Eau Environnement Limoges), Université de Limoges, 123 Avenue Albert Thomas, 87060 Limoges, France. https://orcid.org/0000-0003-4059-5793
Stefano Salvestrini, Department of Environmental, Biological and Pharmaceutical Sciences and Technologies, University of Campania "Luigi Vanvitelli", Via Vivaldi 43, 81100 Caserta, Italy
Mohamed Kebir, Research Unit in Physical and Chemical Analysis in the Fluid and Solid Medium (URAPC-MFS/CRAPC), BP 384 Bou-Ismail, 42000 Tipaza, Algeria
Nacer Belkessa, University Rennes, Ecole Nationale Supérieure de Chimie de Rennes, CNRS, ISCR – UMR 6226, 35000 Rennes, France

1 Introduction

The effluents released by the textile industry, which uses harmful chemicals such as dyes, contain various chromophore groups that have negative effects on flora and fauna. It has been investigated that 1 %–20 % of the world's colorant production is wasted and discarded in the dyeing process, which seriously endangers human health, aquatic ecosystems, and the environment [1]. One of these dyes, methylene blue (MB), depicted in Fig S1, is a toxic, carcinogenic, and non-biodegradable compound, putting both environmental and human health in great peril. In general, it is directly released into natural water resources, posing a threat to human and animal health [2].

To deal with this problem, various wastewater treatment techniques have been investigated, including physical technologies: adsorption on activated carbon, ultrafiltration, reverse osmosis, coagulation with chemical components and ion exchange on synthetic absorbents. However, these methods are not destructive, as they simply transport organic substances from the water to other phases, effectively creating additional contamination. Thus, less costly alternative treatments are required for final wastewater treatment and regeneration of absorbent materials [3].

As a result, research has focused on other green and non-toxic processes that mineralize pollutants, such as heterogeneous photocatalysis, which relies on using nanostructured semiconductors as catalysts to oxidize organic molecules [4]. Among nanoparticles exhibiting these properties, titanium dioxide (TiO_2), ZnO, and CuO have attracted much attention in the field of photocatalysis [5].

Because of their high efficiency and nanotoxicity, TiO_2 nanoparticles have sparked much interest as a photocatalyst. However, the aggregation of nanoparticles caused by energy reduction restricts the number of active sites on the surface of TiO_2, which results in decreasing its specific surface area [6]. When these nanoparticles are used as photocatalysts for wastewater treatment, such a problem should be considered. A simple solution to this issue is to load TiO_2 nanoparticles on specific supports (i.e., supported clay [7], supported activated carbon [8], and apatite [9]) to improve their dispersion.

Clay comes mainly from raw minerals, with different types of geometry and morphology. They can be used for the disposal and storage of hazardous chemicals, especially for contaminated water remediation. In several industries, clay minerals, such as montmorillonite [10], zeolite [3], and kaolinite [11], have been used as raw materials for hundreds of industrial applications due to their abundant availability and inexpensive nature. Clay is thus used as a promising adsorbent in various adsorption methods thanks to its distinct characteristics and high removal performance [12].

Kaolinite is a clay mineral with a multi-layered structure and an exceptional formula $Al_2Si_2O_5(OH)_4$. It is often used in a variety of sectors and applications: paper [13], ceramics [14], paints [15], cement [16], and wastewater treatment [17]. In this work, we prepared kaolinite/TiO_2 nanocomposites by mixing kaolinite with TiO_2 at well-defined proportions, and they were calcined at a fixed temperature (800 °C) while varying the calcination time. These treatments were chosen to investigate their effects on the structural and catalytic properties of the clay minerals, particularly in the context of their application as supports for TiO_2 in photocatalysis for removing methylene blue (MB) dye from aqueous solution.

The primary objective of this study was to elucidate how the different treatment conditions influence the physicochemical properties of the clay samples and their suitability as support for TiO_2. Systematic analysis of the structural changes induced by these treatments and evaluation of their impact on the photocatalytic performance were conducted. Valuable insights can be gained for the rational design of efficient photocatalytic materials.

2 Materials and methods

2.1 Materials

Titanium (IV) isopropoxide (TIP) ($C_{12}H_{28}O_4Ti$; 98 %), ethanol (C_2H_6O; 96 %), nitric acid 65 %, HCl, and NaOH were purchased from Sigma Aldrich (Germany). Methylene blue dye was purchased from Biochem (France). A local kaolinite-halloysite clay was collected in Djebel Debbagh mine (Guelma, northeast Algeria) designated DD2. These chemicals were used without any further purification or treatment.

2.2 Clay preparation

Two ways of preparing the support were used. In the first way, natural Kaolinite was ground during 3 and 8 h, noted as **KH2B3** and **KH2B8** respectively. Grinding was carried out in a FRITSCH planetary ball mono mill (Idar-Oberstein, Germany) at a rotation speed of 200 rpm. In the second way, the clay was first calcined at 600 °C for 2 h, then ground for 3 and 8 h: they are labeled **KH2600B3** and **KH2600B8**, respectively After each grinding of the natural kaolinite, sieving was performed using a 100-µm sieve to ensure a homogeneous particle distribution and to enrich the kaolinite phase of interest (Figure 1).

2.3 Synthesis of kaolinite/TiO_2 nanocomposites

The kaolinite/TiO_2 nanocomposites were synthesized using the sol-gel method [18]: 1 mL of TTIP was mixed and stirred for 1 h in 7 mL ethanol at 40 °C, and the pH of the solution was adjusted with the addition of diluted nitric acid to pH = 1.5. The produced sol was applied dropwise to a suspension of 20 mL containing 0.5 g kaolinite. The resultant suspension was agitated for 24 h, washed, and then heated to 80 °C for 24 h to produce the final powder impregnated with TiO_2. Next, this powder was calcined at 450 °C for 2 h at a rate of 5 °C/min.

TiO_2 nanoparticles were synthesized using the same method without adding kaolinite. The synthetized samples were noted as **KH2** (raw kaolinite), **KTB3**, **KTB8**, **KT600B3**, **KT600B8** and TiO_2 (Figure 1).

2.4 Characterization of kaolinite/TiO_2 composite

The samples were examined using X-ray diffraction (XRD) on a PANALYTICAL (Almelo, Netherlands) diffractometer with

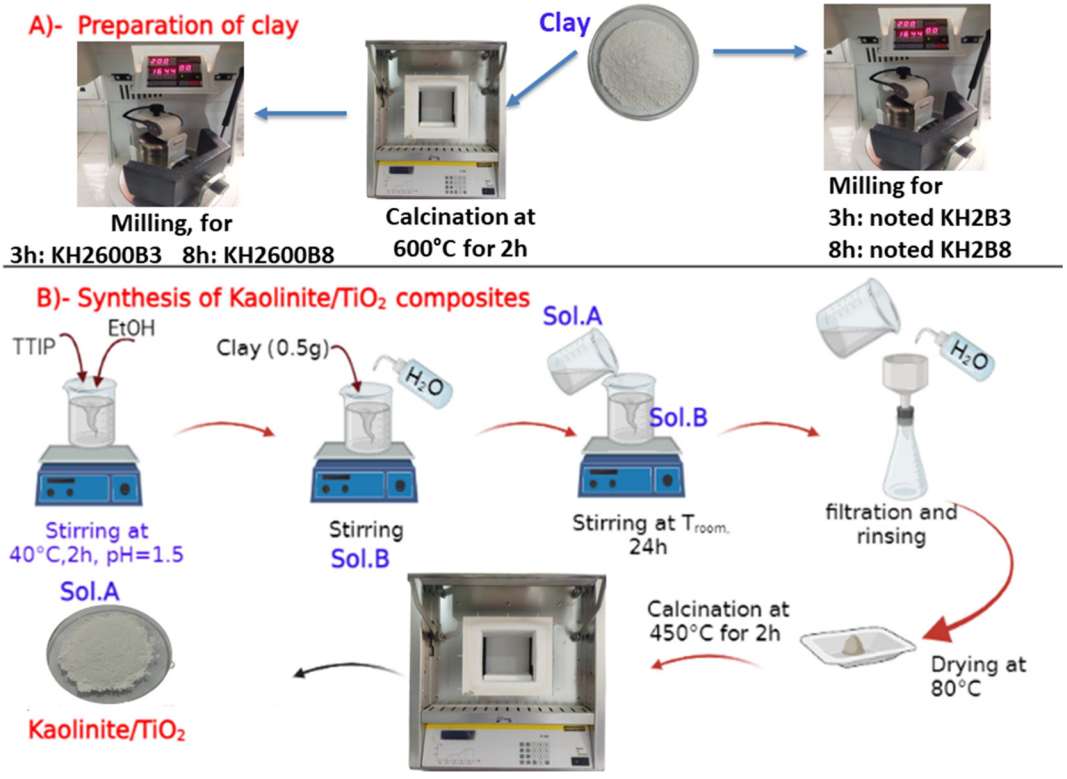

Figure 1: Preparation and synthesis of kaolinite-halloysite and Kaolinite-Halloysite/TiO_2.

Cu Kα radiation. The structural morphology and element analysis of kaolinite-TiO_2 composites were investigated using a JEOL JSM-7610F Plus emission scanning electron microscope (UHR-FESEM) (Tokyo, Japan). Infrared spectroscopy spectra (diamond ATR) were obtained at room temperature using a Bruker Platinum spectrometer (Billerica, USA) in a 400–4,000 cm^{-1} range. The UV-visible absorption spectra (UV–vis DRS) of the samples were obtained using a UV–Vis spectrophotometer Agilent Technologies Cary 60 (Penang, Malaysia). Nitrogen adsorption/desorption isotherms were measured at 77 K using the Quantachrome (Boynton Beach, USA) instrument. The pore volume was calculated using the *t*-plot method, and the sample-specific surface area was calculated using the conventional BET (Brunauer–Emmett–Teller) method. The samples were degassed and dehumidified by heating them at 200 °C for 8 h. To evaluate the mineralization of MB the total organic carbon (TOC) content was analyzed using a Shimadzu TOC-VCSH instrument (Japan).

2.5 Point of zero charge (pHzpc)

To determine the pHzpc, pH tests were carried out as follows [19]. The procedure consisted of adding a 0.1 M NaOH or HCl solution to 50 mL of closed flasks containing a 0.1 % NaCl solution to adjust the pH of each flask between 2 and 10 (Fig. S2). In each flask, we added 0.15 g of adsorbent. To determine the final pH, with pH meter-LC-pH-2B (Zhejiang, China), the suspensions was kept at room temperature with continuous stirring for 48 h.

2.6 Adsorption kinetic experiments

The kinetic study of adsorption was carried out by mixing a sample weight of 0.1 g with 100 mL of MB solutions (C_o = 20 mg/L) at 25 °C and pH = 7.6. A given volume was taken at different time intervals. After separating the adsorbent–adsorbate mixture, MB dye concentrations were determined by spectrophotometry 200–800 nm (Agilent, Cary 60 UV–vis). The MB dye concentrations were determined with measurements taken specifically at 665 nm, the absorption maximum for methylene blue. Experimental data of adsorption kinetics were analyzed using the pseudo-first-order (PFO) and pseudo-second-order (PSO) model (Figure 7a) [20], [21].

2.7 Photocatalytic experiments

Methylene blue (MB) photodegradation experiments have been made to evaluate the practical reliability of the obtained composites. All experiments were performed at 25 °C. The reactor is a batch system placed in a chamber, with seven 9 W

UV-A lamps at a wavelength of λ = 365 nm positioned inside the chamber. The distance between the lamps and the beaker is 15 cm. The light intensity used during the experiments is 200 lux. A 100 mL sample of MB solution (20 mg/L) was placed in the beaker, followed by the addition of 100 mg/L of the photocatalyst. First, the solution was stirred by Selecta Multimatic 5 N stirrer (Wertheim, Germany) at 300 rpm in the dark to achieve an adsorption-desorption equilibrium. Then, the suspension was irradiated under the UV light source according to the irradiation time under constant stirring. During this process the samples were regularly taken from the beaker, centrifuged, and the liquid phase analyzed using a UV–vis spectrometer. The photodegradation rate of MB was determined by Equation (1).

$$\text{MB (\%) Photodegradation} = \frac{C_0 - C_t}{C_0} * 100 \quad (1)$$

where C_0 and C_t are the initial concentration of dye in the solution and its concentration at time t, respectively.

3 Results and discussions

3.1 XRD spectrum

Figure 2a shows the XRD spectrum of KH2. The presence of the kaolinite (JCPDS card No. 96-900-9235) and halloysite sheets was identified (JCPDS Card No. 29–1487) respectively [22] [23]; quartz was present in small amounts. Intensive milling can induce structural changes in halloysite crystals. This could include amorphization, crystal defects, and even polymorphic transitions. Such alterations in crystal structure can manifest as shifts in peak positions or the disappearance of certain peaks in the XRD pattern, causing a decrease in peak intensity after about 8 h [24]. However, when the kaolin is calcined at 600 °C, only a dome is noticed, which characterizes the transformation of kaolinite into metakaolinite form. Metakaolinite is characterized by a disordered crystal structure. As a result, it becomes amorphous, i.e., loses its regular crystalline arrangement and becomes structurally disordered [25].

Figure 2b represents the XRD diagram of the synthetized TiO_2 and kaolinite/TiO_2 composites respectively. The XRD spectra of TiO_2 revealed the presence of three phases, the peaks at 25.3°2θ, 36.9°2θ, 37.7°2θ, and 48.0°2θ (JCPDS card No. 96-900-9087) were attributed to anatase phase. Some peaks at 27.4°2θ, 36.1°2θ, 39.2°2θ, and 44.1 °2θ (JCPDS card No. 96-900-1682) were assigned to rutile phase, and the peak at 30.80°2θ were attributed to brookite phase (JCPDS card No. 96-900-4138) [26].

A progressive decrease in the intensity of kaolinite-specific reflections was observed due to the immobilization of TiO_2 in the crystalline structures of kaolinite-TiO_2 composites with varying grinding times, with or without heat treatment of the clay [27]. Once TiO_2 is immobilized in the kaolinite crystal structure, the resulting composite can exhibit useful synergistic properties, such as better stability and enhanced photocatalytic reactivity. A series of TiO_2 characteristic peaks at around 25.3°2θ, 38.3°2θ, 48.1°2θ 53.9° 2θ, 55.1°2θ and 62.7°2θ matched the TiO_2 anatase crystals in a planar array. It is possible to infer that the presence of kaolinite speeds up the synthesis of anatase and prevents it from turning into rutile. [28]. According to the small size of TiO_2 nanoparticles, the pure TiO_2 reference exhibits the anatase phase's distinctive widened diffraction peaks (JCPDS card No. 96-101-0943) [29] [30] [31]. After the incorporation of titanium dioxide, the samples showed an increase in the

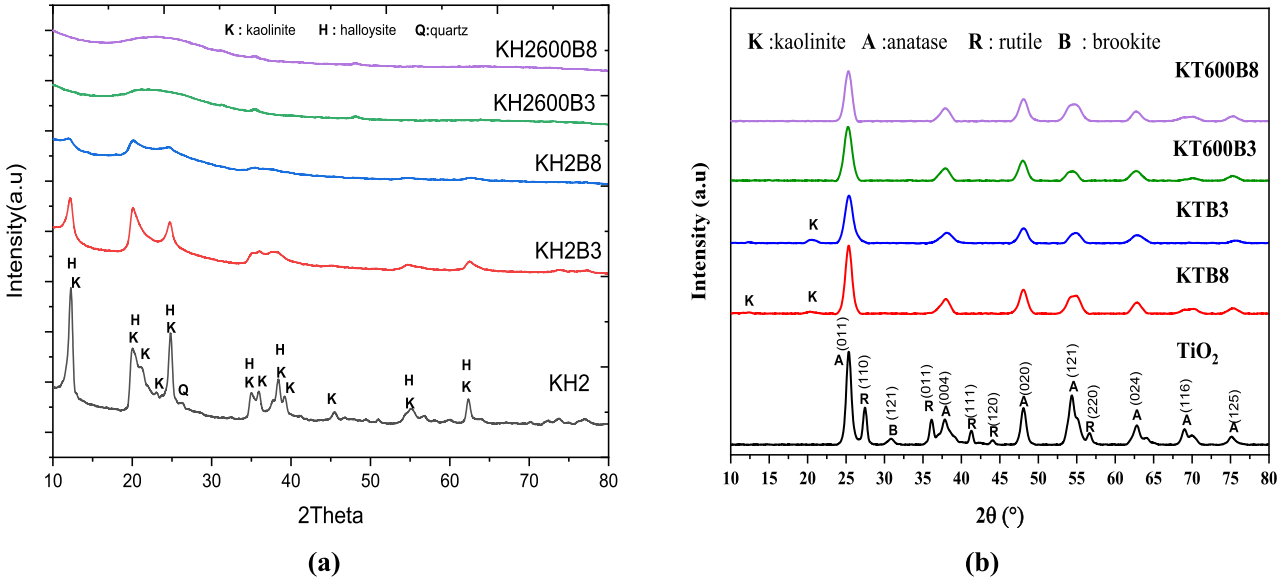

Figure 2: XRD of (a): kaolinite samples after various treatments and (b): kaolinite/TiO_2 composites.

signal at 2θ = 25°, possibly due to the anatase phase of TiO_2, which overlaps the signal of kaolinite [32]. However, no distinct kaolinite features were observed in the kaolinite/TiO_2 composite samples after calcination for KT600B3 and KT600B8, which could be attributed to the loss of stacking in the kaolinite layers and the completion of the dehydroxylation reaction during this period; kaolinite was in amorphous metakaolinite form, so no obvious peak was shown in Figure 2a. It is widely reported that smaller grain sizes result in increased photocatalytic activity. Smaller grains can reduce surface defect density, promote uniform adsorption of reactive molecules, and minimize unwanted charge carrier recombination reactions. According to Scherrer's formula [33], the average grain size of TiO_2 and TiO_2 nanoparticles in kaolinite is 18 and 10 nm, respectively.

The diffraction peaks of the kaolinite/TiO_2 composites correspond well with those of the TiO_2 anatase phases and kaolinite, indicating that the kaolinite structure is preserved during the TiO_2 nanoparticle introduction. Meanwhile, the diffraction intensities of kaolinite in kaolinite/TiO_2 composites dropped, showing that TiO_2 was successfully loaded on the surface of kaolinite [34].

3.2 SEM and EDX analysis

The nano-morphology was revealed with an in-lens secondary electrons detector, while the material contrast was obtained with a retractable backscattered electrons detector. In the first mode, using secondary electrons, clear high-resolution images provided the shape and the size of TiO_2 particles.

The samples were directly observed in their natural state, without prior metallization (no carbon layer evaporation nor conductive metal sputtering). Different electron optical parameters were selected in the second mode, namely backscattered electrons. Images at relative low magnifications (2500× for the large ones and 10k× for the inserts) were performed to study the spatial distribution of TiO_2. A higher accelerating voltage of 7 kV and larger probe current at a shorter working distance of 6 mm made the acquisition of a sharp atomic number contrast possible. This mode of imaging allowed us to track the presence of TiO_2 particles onto the clay. Titania appears with a brighter contrast because titanium is heavier than any other element present in the as-prepared nanopowders. Figure 3a shows that the KH2 raw clay has a mesoporous mixture between sheet-like kaolinite, which is partially light-covered, and halloysite, which is of tubular morphology [35]. In the case of pure TiO_2 (Figure 3b), it was revealed that the particles are randomly distributed, and they also contain small spheres with the formation of agglomerates. Based on the SEM analyses of the morphology of clay/TiO_2 nanocomposites, it can be shown that well-distributed, but not uniformly sized, spherical TiO_2 particles form on the surface of the clay, with an average size of approximately 10 nm. The adsorption

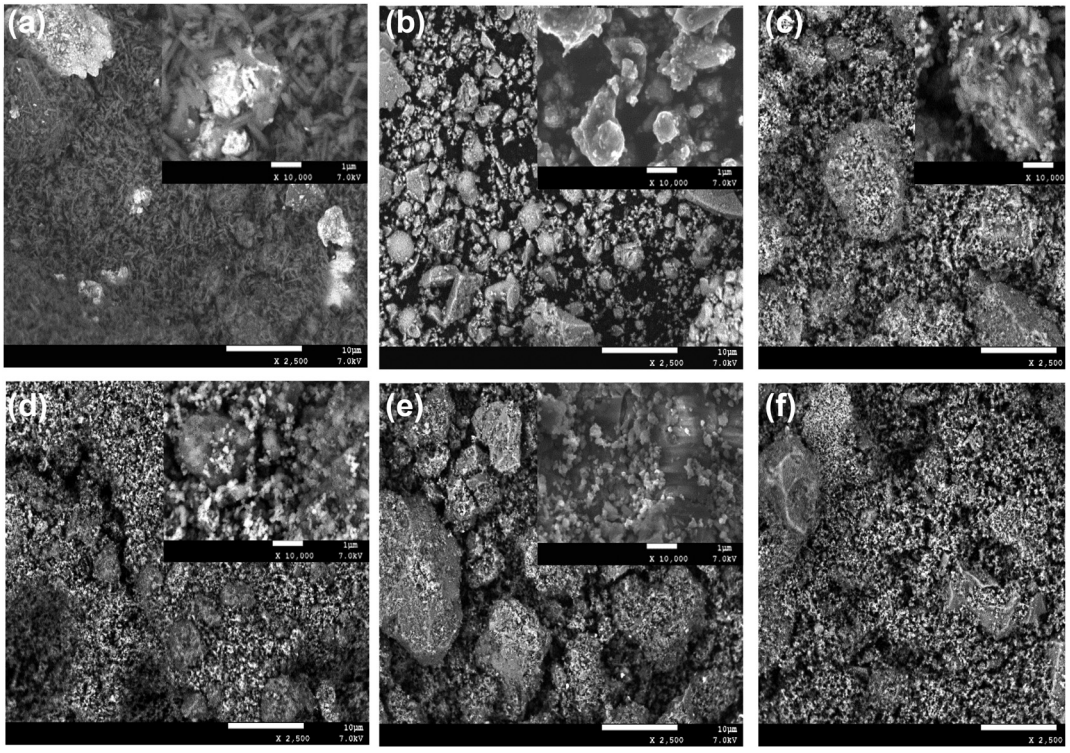

Figure 3: SEM images of composites (a) KH2, (b) TiO_2, (c) KTB3, (d) KTB8, (e) KT600B8 and (f) KT600B3.

capacity and photocatalytic activity of the nanocomposites might change due to the varying degrees of dispersion of TiO_2 particles on the clay surface [28]. The KT600B3 and KT600B8 nanocomposites showed significant changes compared to the other two nanocomposites, KTB3 and KTB8, indicating that calcination causes the structure of the clay to become more disordered.

3.3 BET analysis

The nitrogen adsorption/desorption isotherms of samples are presented in Figure 4; the samples' mesoporous adsorbents correlate to type IV's adsorption isotherm. This indicates that mesoporosity makes up most of the overall porosity, comparable to holes that resemble slits in layered materials. Table 1 shows that the BET surface area of all solid samples [36] Increasing the calcination temperature and grinding time caused a decrease in the specific surface area, and an increase in the size of kaolinite/TiO_2 crystallites. The dried catalyst KTB3 had the highest specific surface area and

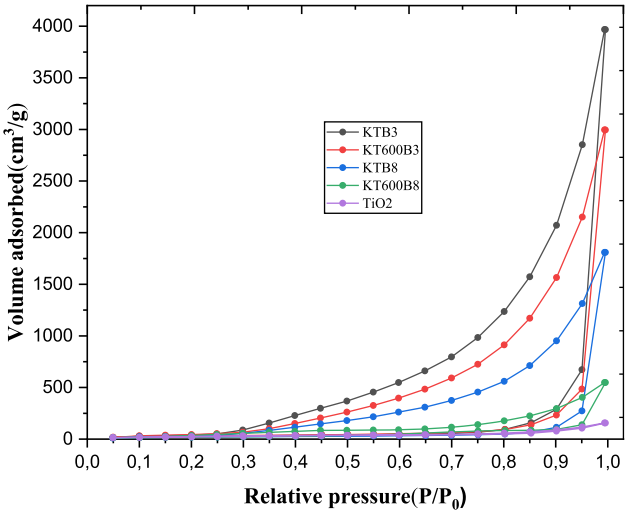

Figure 4: Nitrogen adsorption/desorption isotherms of samples at 77 °K.

Table 1: Mean pore diameter, pore volume and specific surface area of solid samples.

Samples	Mean pore diameter (nm)	Pore volume (cm^3/g)	BET surface area (m^2/g)
KTB3	8.85	4.715	197.9
TiO_2	2.82	0.863	72.52
KT600B3	7.43	0.630	106.57
KTB8	8.29	0.223	91.77
KT600B8	6.82	0.2834	81.4

the catalysts calcined at 600 °C (KT600B3, KT600B8) and KTB8 milled at 8 h had the smallest crystallite size [37].

3.4 Infrared spectrum (ATR)

Figure 5 shows the ATR spectrum (vibrational bands and interfaces of interaction) for each sample. For KH2, the bands at 1,036 cm^{-1} and 1,008 cm^{-1} correspond to the stretching vibrations of the Si–O structural lattice (Si–O–Si and O–Si–O). The other bands at 1,117 cm^{-1} are due to the Si–O stretching vibration at the apex and the out-of-phase stretching vibration of the inner surface hydroxyl, respectively [38]. The deformation band at 428 cm^{-1} corresponds to the Si–O groups [39]. The stretching vibration of the inner surface hydroxyl (OH), which is seldom ever affected by intercalation, is thought to be responsible for the absorption bands at 3691, 3620, 3658, and 910 cm^{-1}. O–Al-translational OH vibration causes the bands at 790, 744, and 685 cm^{-1}, whereas Si–O-vibration Al is responsible for the bands at 534 and 462 cm^{-1}. Kaolinite/TiO_2 nanocomposites exhibit the stretching and bending vibrations of water molecules adsorbed groups at 1,632 cm^{-1} [40]. Keep in mind that there is no difference in the hydroxyl vibration peaks of kaolinite before and after loading. The stretching vibration of Ti–O is responsible for the peaks in the spectra between 400 and 900 cm^{-1}, which are a strong sign of the existence of TiO_2. The peak at 950 cm^{-1}, which is attributable to the antisymmetric stretching vibration Si–O–Ti, shows that titanium dioxide and kaolinite were combined chemically to produce the kaolinite/TiO_2 composite [41] [42]. The change of kaolinite to metakaolinite also results in a shift in the band structure that manifests as structural dehydroxylation and metakaolinite production, which causes a shift in the Al^{+3} coordination of the octahedral area 1250–400 cm^{-1}. Amorphous SiO_2 was identified as the source of broad bands with maxima at 950 and 1,120 cm^{-1}. Metakaolinite was created by calcining kaolinite at 600 °C. Amorphous silica was also seen vibrating between 1,200 and 1,050 cm^{-1} [43]. The faster elimination of vibrations perpendicular to the mineral layers was found for KTB3 and KTB8 in the Si–O stretching zone. Mechanical treatments such as grinding have the most impact on these bands, even if XRD results show that the kaolinite was converted into a non-crystalline substance. As a result, this band might represent the whole amount of silica. The intensity of Si–O–Al oscillations was significantly reduced, indicating that the bond between the octahedral and tetrahedral layers was easily deteriorated. It was observed with treatment time that the Si–O bending bands at 429 and 462 cm^{-1} gradually decreased. Even after a prolonged treatment period, the band at 429 cm^{-1} did not fade [44]. When grinding kaolin

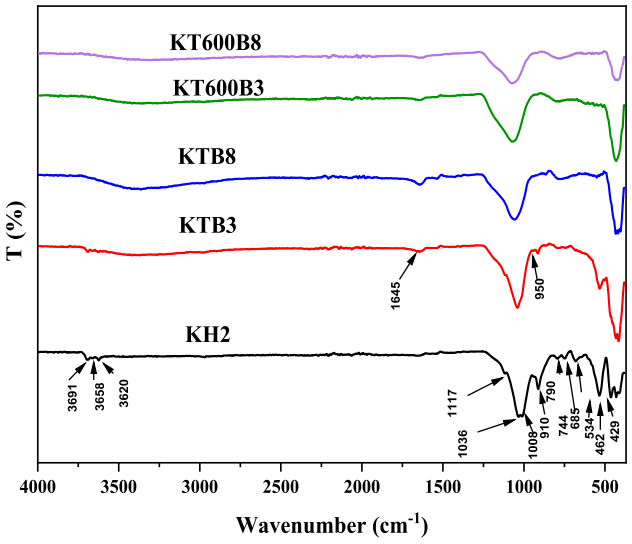

Figure 5: Infrared spectrum of kaolinite/TiO_2 composites.

during different times, the 3691, 3620, 3658, and 910 cm^{-1} absorption bands of the inner surface hydroxyl groups decreased with the grinding times [45].

In the low-wavenumber region, hydroxyl deformation modes were observed between the surface water molecules formed by breaking Si–O or Al–O–Si bonds (internal hydroxyls). In parallel with the weakening of the stretching vibration band, the intensities of these bands also decreased during grinding. Due to its stability after milling, the band at 1,036 cm^{-1} is thought to reflect the overall amount of silica present and can be therefore used as a reference for comparing different samples.

Figure S4 shows the IR spectra obtained for the pure TiO_2; the band at 428 cm^{-1} is attributed to the bending vibrations of the framework bonds Ti–O and Ti–O–Ti [46].

Methine (–CH–) and methylene (–CH_2–) groups are represented by the tiny peaks at 2972 and 2871 cm^{-1}, respectively. The characteristic peak at 1,650–1,597 cm^{-1} is associated with the stretching frequency of carboxylate (–COO), indicating that the organic component does not completely evaporate at 450 °C [47].

3.5 DRS UV–vis spectra

Figure 6 shows the DRS UV–vis spectra of pure TiO_2 and the various kaolinite/TiO_2 composites. The band gap calculation is most important from the point of energy conversion efficiency. The optical band gap of the photocatalyst was estimated using equation of Tauc:

$$\alpha h\nu = A(h\nu - E_g)^n \quad (2)$$

where A represents a constant, $h\nu$ is photon energy, α is absorption coefficient, E_g represent forbidden band, and n = ½ (for a direct transition) or n = 2 (for an indirect transition).

The intersection of the linear part of the Tauc plot $(\alpha h\nu)^{½}$ with the energy-axis gives the value of the band gap [48]. The optical bandgap energy values of the nanomaterials prepared (TiO_2, KTB3, KTB8, KT600B3, and KT600B8) were 2.93, 3.13, 3.14, 3.14 and 3.14 eV respectively. This finding implies that kaolinite causes the absorption edge of TiO_2 to shift to a higher energy region. On the one hand kaolinite may increase catalytic activity by delaying the recombination of separate charges produced by UV radiation in the TiO_2 crystal lattice [49]. Consequently, the presence of SiO_2 in the kaolinite/TiO_2 composites leads to slightly improving the ability of TiO_2 nanoparticles to absorb light as long as they form a chemical bond with SiO_2 [50].

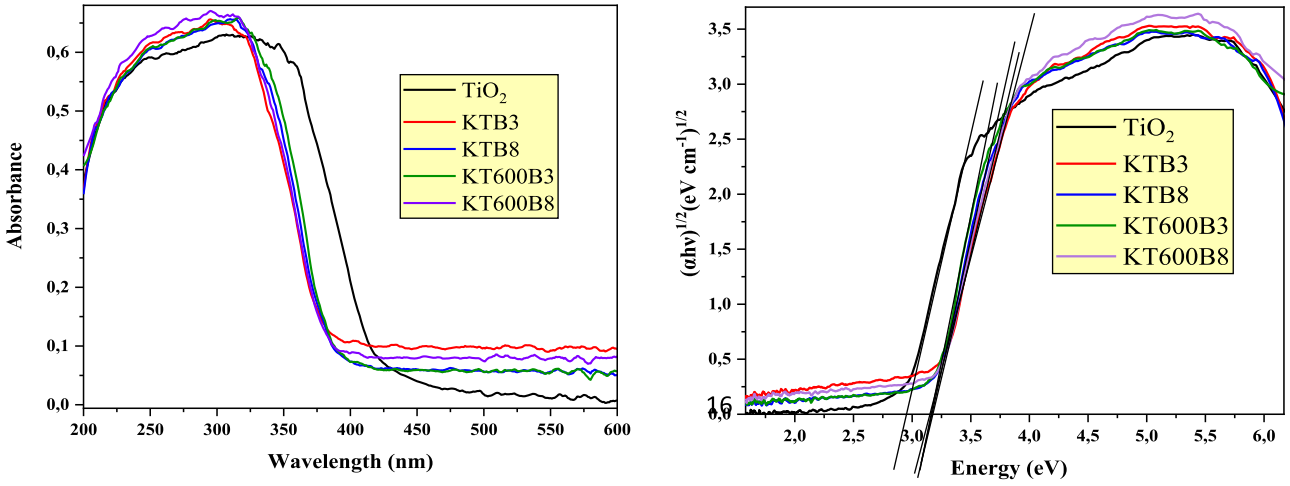

Figure 6: DRS UV–vis spectra of pure TiO_2 and kaolinite/TiO_2 composites.

3.6 Adsorption study

3.6.1 Adsorption kinetics

The study of the adsorption kinetics of MB in an aqueous solution is demonstrated by adsorption rate curves and modelled by the pseudo-first-order and pseudo-second-order kinetic plots expressed in Eqs. (3) and (4), respectively [51] [52].

$$\frac{dq_t}{dt} = k_1(q_e - q_t) \tag{3}$$

$$\frac{dq_t}{dt} = k_2(q_e - q_t)^2 \tag{4}$$

Integrating both equations, the corresponding nonlinear forms are obtained as the following equations:

$$q_t = q_e\left(1 - e^{-k_1 t}\right) \tag{5}$$

$$q_t = \frac{q_e^2 k_2 t}{1 + k_2 q_e t} \tag{6}$$

where k_1 and k_2 are the pseudo-first-order and pseudo-second-order rate constant, respectively. Physically, q_e represents the adsorption capacity at equilibrium, while k_1 and k_2 reflect the rate of adsorption: a higher rate constant indicates a faster approach to equilibrium. The pseudo-first-order model is often applied when the adsorption process is dominated by diffusion or physical interactions on a homogeneous surface. On the other hand, the pseudo-second-order model is widely used for systems where chemisorption, such as bond formation or electron exchange, governs the kinetics [53]

Figure 7a revealed that adsorption equilibrium was reached after 60 min for the majority of the prepared materials, and the amount of adsorbate on the surface reached a plateau, indicating that the material surface is saturated and no further adsorption is possible, and demonstrating that the adsorption kinetics of the dye on the synthetic material is relatively rapid. To further evaluate the adsorption kinetics of MB, kinetic rate constants (k_1 and k_2), equilibrium adsorption capacities (q_e), and correlation coefficients (R^2) were determined. The results of the pseudo-first-order and pseudo-second-order models are presented in Table 2. According to the results obtained, the kinetics are described by the pseudo-second-order model, which is in agreement with the work reported by Tran et al. [54]. However, the novelty of our study lies in applying this model to the specific TiO_2/kaolinite composite synthesized in this work, which has unique physicochemical properties influenced by its preparation method. These results provide new insights into the adsorption behavior of TiO_2/clay-based composites and their potential for environmental applications, further validating the consistency of pseudo-second-order kinetics in clay-supported adsorption systems. In addition, the calculated q_e values were closer to the experimental values obtained, which explains why the adsorption kinetics of the dyes on the prepared materials follow the PSO models [55].

3.7 Adsorption isotherm

The data were modeled using the two most well-known isotherm models, Freundlich (Eq. 7) and Langmuir (Eq. 8), to define the interaction of methylene blue molecules with the KTB3 surface and to study the distribution properties in liquid and solid phases. Equations 7 and 8 provide expressions of the non-linear relationship of these isotherm models [52].

$$q_e = K_F C_e^{1/nF} \tag{7}$$

$$q_e = \frac{q_m K_L C_e}{1 + k_L C_e} \tag{8}$$

In the formula, C_e is the equilibrium concentration of methylene blue (mg/L), n_F and K_F are the Freundlich constants, q_e and q_m are the amount of MB adsorbed at equilibrium and the maximum adsorption capacity, respectively. K_L (L/mg) is the Langmuir equilibrium constant. Applying Eq. (8), we can determine the maximum amount of MB adsorbed by the nanocomposite (q_m), which is around 29.73 mg/g (Figure S4). Moreover, the adsorption rate decreases with increasing grinding time and degree of kaolinite calcination. The characteristic constants of each system were determined and listed in Table S1. The methylene blue adsorption isotherm shows that the best correlation of experimental results is obtained with the Langmuir model (R^2 = 0.99) Table S1 [56].

3.8 Photocatalytic experiments

The kinetics and rate constant of methylene blue photodegradation have been studied using the Langmuir-Hinshelwood equation (Eq. 9) obeying first order kinetics [57]:

$$r = -\frac{dC_t}{dt} = \frac{kKC_t}{1 + KC_t} \tag{9}$$

where k [mg/(min L)] and K (L/mg) correspond to the photocatalytic rate constant and the adsorption equilibrium constant, respectively, and C_t is the concentration at time t (min).

When:

- KC_t >>1, so the value of $1 + KC_t \approx KC_t$
- $KC_t \ll 1$, to be a result, the denominator $1 + KC_t \approx 1$

Using these two mathematical theorems and the low dye concentrations used in photocatalysis, the Langmuir-Hinshelwood equation has been created.

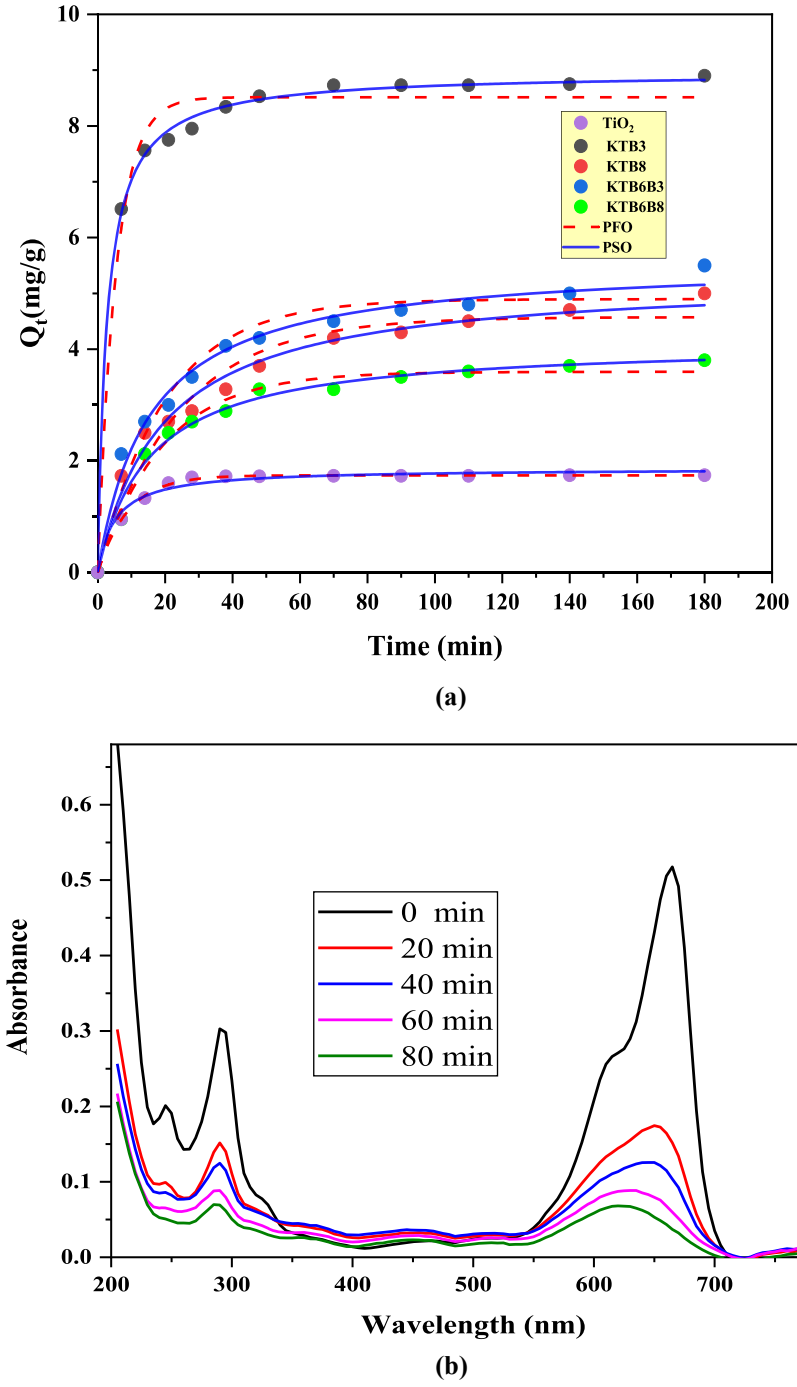

Figure 7: Kinetic study (a) for all the materials used at T = 25 °C, Co = 20 mg/L, pH = 7.6 and S/L = 0.1/mL, (b) UV–vis spectra of methylene blue photodegradation by KTB3 as a function of time.

Table 2: Kinetics parameters for the adsorption of MB.

Samples	PSO model			PFO model		
	R^2	q_e (mg/g)	k_2 (g/mg × min)	R^2	q_e (mg/g)	k_1 (min^{-1})
KTB3	0.99	8.95	0.04	0.98	8.51	0.183
KTB8	0.98	5.29	0.009	0.98	3.59	0.051
KT600B3	0.98	5.59	0.011	0.95	4.89	0.049
KT600B8	0.98	4.12	0.015	0.98	3.59	0.051
TiO_2	0.98	1.86	0.105	0.99	1.73	0.111

$$-\frac{dC_t}{dt} = k_1 C_t \tag{10}$$

$$k_1 = k \times K \tag{11}$$

The integral of the equation result in:

$$ln\ C_t = -k_1 t + A \tag{12}$$

$$C_t = Be^{-k_1 t} \tag{13}$$

where k_1 (min^{-1}) is the first-order model's rate constant.

When t = 0 and $C_t = C_0 = B$, as seen below, the nonlinear equation can be simplified:

$$C_t = C_0 \times e^{-k_1 t} \tag{14}$$

This pseudo-first-order model was used to determine the correlation coefficient (R^2). The rate and mechanism of subsequent adsorption and degradation processes could be used to characterize the model of methylene blue degradation kinetics [18]. The results are represented in Table 3.

The experimental results show that supporting TiO_2 on kaolinite results in an improvement in MB removal efficiency from 71 % to 98 % for pure TiO_2 and KTB3, respectively (Figure 8a). This result was explained by the large specific surface area of the clay [58]. Supporting TiO_2 on kaolinite can provide more adsorption and photocatalytic active sites for the decomposition of organic molecules, which confirms the synergy effect between both phenomena [59]. KTB3 has better photocatalytic performance; after 80 min, it eliminates 95 % because the grinding of kaolinite can provide significantly more adsorbent active sites, therefore, greater photocatalytic performance. On the other hand, the other composites have a less efficient photocatalytic capacity due to the destruction of the kaolinite structure by calcination at 600 °C and the increase in grinding time. The kaolinite/TiO_2 composite performs better methylene blue degradation than pure TiO_2 [38].

3.9 Influence of photocatalyst amount

A series of studies were conducted with varying dosages of catalysts at an initial dye concentration C_o = 21 mg/L to investigate the dose effect of KTB3 on MB photodegradation at pH = 7.6. Figure 8b shows that the different catalyst doses ranged from 0.2 to 1.5 g/L. The degradation efficiency increases proportionally with photocatalyst dose, up to the optimum of 1 g/L. This is most likely due to an increase in the number of adsorbed MB molecules, which is directly related to the number of KTB3 particles when the photocatalyst dose increases, as well as an increase in the number of electrons excited to produce radicals (·OH) at the optimal dose of 1 g/L, which depends on the operating conditions. Increases in photocatalyst doses have a negative impact on degradation efficiency. The decrease in the efficiency of degradation beyond 1 g/L can be attributed to the shielding effect of an excess of KTB3 particles and the loss of light caused by diffusion at the saturation of the absorption photons [60].

Table 3: Kinetics parameters of nanocomposites for the photocatalysis of MB.

Model	PSO			MB (%) Photodegradation
	C_0 (mg/L)	K (min^{-1})	R^2	
KTB3	11.48	0.056	0.964	98
KTB8	13.48	0.013	0.964	86
KT600B3	12.40	0.022	0.974	91
KT600B8	13.76	0.011	0.960	81
TiO_2	14.82	0.006	0.943	71

3.10 Effect of dye concentration

In this section, a series of MB solutions with different concentrations from 12 mg/L to 44.5 mg/L have been prepared. It is evident that the rate of photodegradation is affected by dye concentration. It was investigated that degradation yield decreases from 98 to 57 % when the dye concentration is increased from 21.38 to 44.5 mg/L (Figure 8c). The rate of degradation is proportional to the generation of ·OH radicals on the catalyst's surface and the likelihood that the ·OH radicals will react with the dye molecule. This means the rate at which the dye is degraded depends on the amount of hydroxyl radicals (·OH) generated on the catalyst surface. The more ·OH radicals generated, the higher the rate of degradation. The photodegradation kinetics are rapid at low initial concentrations (Figure 8c) due to the small number of MB molecules present in the solution. This results in high availability of photogenerated active species, which are responsible for photodegradation. When the initial dye concentration is high, the path length of the photon entering the solution also decreases. Thus, the efficiency of photocatalytic degradation decreases, but at low concentrations, the opposite effect is observed, increasing photon absorption by the catalyst [36]. The large amount of adsorbed dye can also have a competing effect on the adsorption of oxygen and ·OH to the catalyst surface.

3.11 Effect of pH, extent of mineralization and scavenging effect

The pH is one of the most critical parameters influencing the photocatalytic process. Figure 8d depicts the effect of pH (from 2 to 10) on MB adsorption on KTB3 (at a starting concentration of MB of 20 mg/L and an adsorbent dosage of 1 g/L)

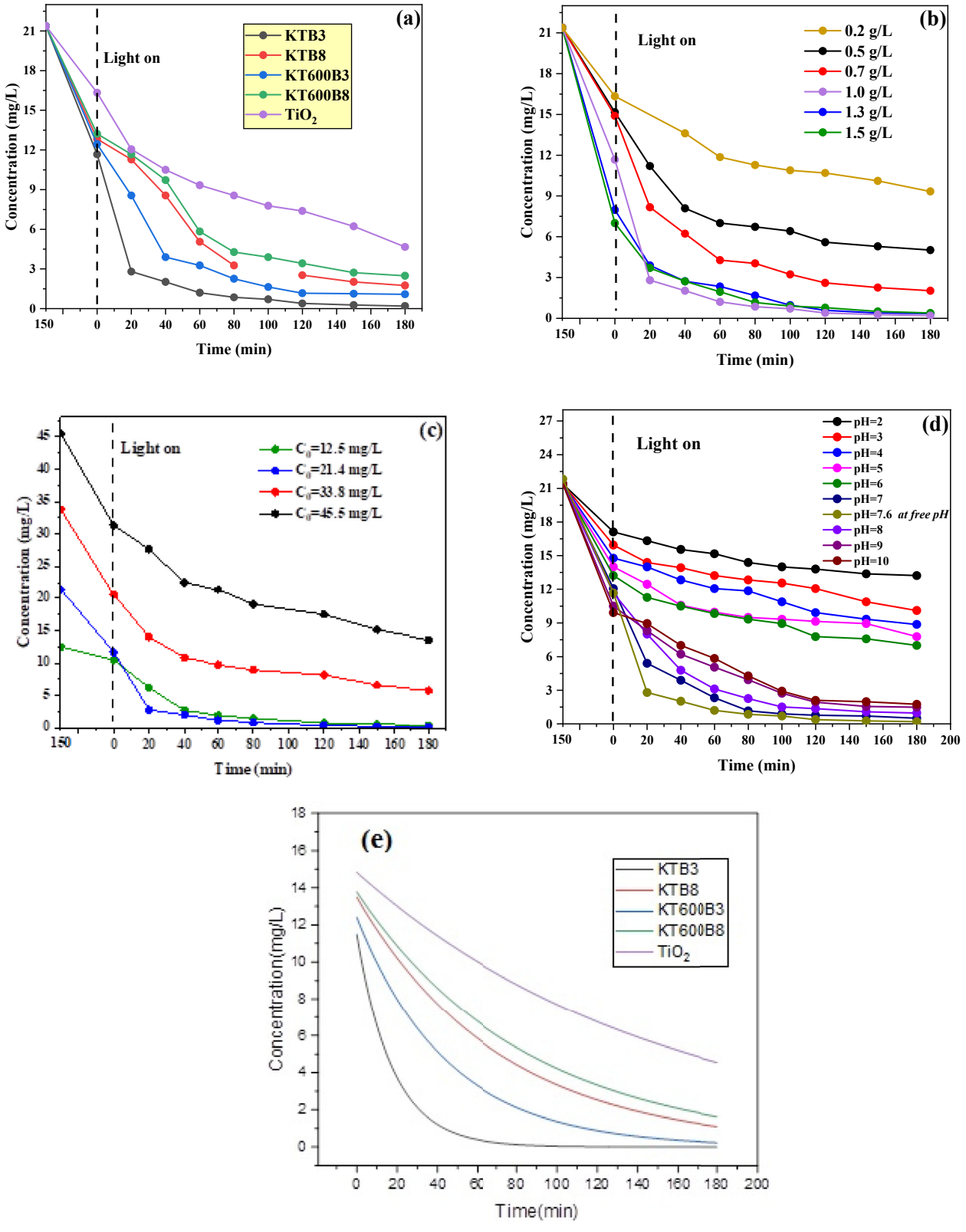

Figure 8: The effect of photocatalysis composites (a) effect of photocatalysis dose (b) effect of initial dye concentration (c) pH effect (d) and first order kinetic (e) on removal of MB with KTB3.

when HCl (0.1 M) or NaOH (0.1 M) are added. The increased pH of the adsorbent medium modifies the clay mineral surface, which may be responsible for the progressive increase in methylene blue adsorption, and the protonated catalyst surface may strongly attract positively charged dye molecules, resulting in superior photocatalytic degradation. According to the literature, photocatalytic activity increases with increasing pH; however, an excessive amount of H^+ in the solution causes a decrease in the degradation [61]. Figure 8d shows that when the pH increased from 2 to 7, the degradation of MB increased progressively from 22.7 % to 95.8 % and then decreased to 82.3 % beyond pH 10. This is caused by the electrostatic attraction between the positively charged catalyst and the MB molecules [61]. It can also be explained by the presence of OH^- ions in solution, which promote the creation of ·OH radicals, encouraging photodegradation.

The mineralization efficiency was determined using the following equation:

$$R\,(\%) = \frac{TOCi - TOCf}{TOCi} \times 100 \tag{15}$$

The total organic carbon (TOC) analysis revealed a significant difference in mineralization efficiency between the tested samples. The KTB3 catalyst demonstrated exceptional performance, achieving a mineralization rate of 93 %, compared to 63 % for TiO_2 alone. These findings highlight the superior capability of KTB3 in degrading and mineralizing organic compounds, confirming its potential as an efficient catalyst for advanced treatment applications.

As concerns the scavenging experiments, the results in Figure 9 showed a decrease in photocatalytic degradation when specific scavengers, such as isopropanol (IPA), silver nitrate ($AgNO_3$), and ethylenediaminetetraacetic acid (EDTA) (Figure 9), were introduced in the methylene blue degradation reaction using the TiO_2/kaolinite composite KTB3. This reduction in degradation is explained by the ability of these scavengers to neutralize key reactive species involved in the photocatalysis. IPA acts as a hydroxyl radical (·OH) scavenger, limiting their contribution to pollutant oxidation. $AgNO_3$, as an electron acceptor, traps electrons in the conduction band (e^-), thereby reducing the formation of superoxide radicals (O_2·–). EDTA, as a hole (h^+) scavenger, prevents direct oxidation reactions initiated by these holes [62] [63]. The observed decrease in degradation supports the central role of these reactive species (·OH, h^+, O_2·–) in the photocatalytic process, and the scavenger effect limits their availability, reducing the overall efficiency of the reaction.

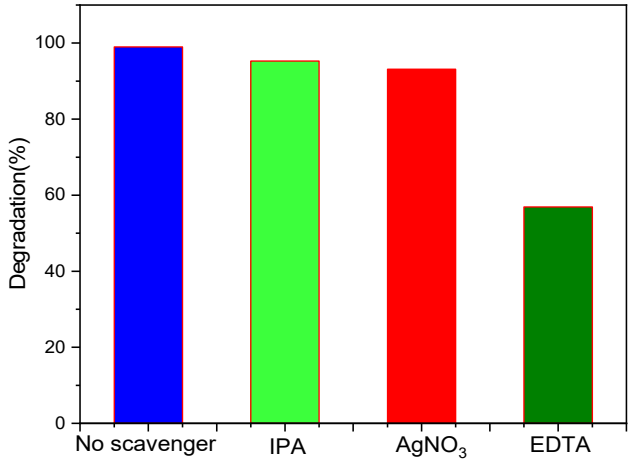

Figure 9: Photocatalytic removal of MB in presence of several scavengers using KTB3.

3.12 Mechanism of kaolinite/TiO_2 assisted photocatalytic degradation

The mechanism of photocatalysis by TiO_2 has already been described in depth in the literature [65] [66]. When an aqueous TiO_2 dispersion is exposed to light energy above its bandgap energy (3.2 eV), conduction band electrons (e^-) are produced, triggering photocatalytic activity (Figure 10), holes can combine with OH^- or H_2O and become $OH^•$ radicals as a result. They then react with H^+ to produce a hydrogen dioxide radical ($HO_2^•$, hydroperoxyl).

$$\text{kaolinite}/TiO_2\ \text{composites} + h\nu \rightarrow TiO_2\,(h^+ + e^-) \tag{16}$$

Reaction involving valence band h^+

$$(h^+) + H_2O \rightarrow +^{\cdot}OH + H^+ \tag{17}$$

$$(h^+) + OH^- \rightarrow +^{\cdot}OH \tag{18}$$

$$(h^+) + 2H_2O \rightarrow +H_2O_2 + 2H+ \tag{19}$$

Reaction involving conduction band e^-

$$(e^-) + O_2 \rightarrow O_2^- \tag{20}$$

$$O_2^{\cdot-} + H^+ \rightarrow HO_2^{\cdot} \tag{21}$$

$$(e^-) + HO_2^{\cdot} \rightarrow TiO_2 + HO_2^- \tag{22}$$

$$TiO_2\,(e^-) + O_2^{\cdot} + 2H^+ \rightarrow TiO_2 + H_2O_2 \tag{23}$$

$$TiO_2\,(e^-) + H_2O_2 \rightarrow TiO_2 + {}^{\cdot}OH + OH^- \tag{24}$$

$$O_2^{\cdot-} + H_2O_2 \rightarrow \cdot OH + OH^- + O_2 \tag{25}$$

$$2HO_2^{\cdot} \rightarrow O_2 + H_2O_2 \tag{26}$$

Photoholes have a considerable potential by combining with the ·OH that predominates in aqueous solutions.

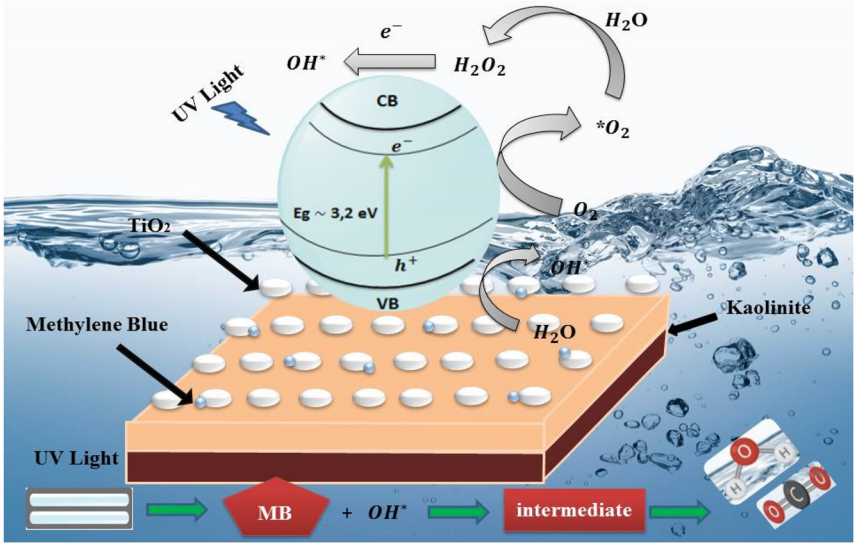

Figure 10: Proposed mechanism of kaolinite/TiO_2 composites assisted photocatalytic degradation of MB under UV-light [64].

$$O_2^{-}/h^+/{}^{\cdot}OH + MB \rightarrow CO_2 + H_2O/\text{by-product} \quad (27)$$

Upon UV irradiation, the TiO_2 in the kaolinite/TiO_2 composite absorbs photons (hν), which generate electron-hole pairs (e– and h^+) (Equation 16). The photoexcited holes (h^+) in the valence band participate in several reactions, including the oxidation of water to produce hydroxyl radicals (·OH) (Equations 17 and 18). In the presence of excess water, these holes can also produce hydrogen peroxide (H_2O_2) (Equation 19). On the other hand, the electrons (e–) in the conduction band reduce molecular oxygen (O_2) to form superoxide radicals (O_2^-) (Equation 20), which, in turn, react with protons (H^+) to form hydroperoxyl radicals (HO_2·) (Equation 21). These reactive species (·OH, O_2^-, and HO_2·) are capable of decomposing organic pollutants like methylene blue (MB) into non-toxic by-products, such as CO_2 and H_2O (Equation 27). Additionally, the superoxide radical can also react with hydrogen peroxide to form hydroxyl radicals and oxygen (Equations 23 and 24), further enhancing the degradation process [67].

The grinding of kaolinite improves the photocatalytic performance by increasing the specific surface area, dispersion, and adsorption capacity of the TiO_2, which helps to improve the overall reactivity and efficiency of the composite in water treatment applications. These results demonstrate the potential of kaolinite/TiO_2 composites for more efficient and cost-effective photocatalytic water. The photocatalytic performance of the synthesized kaolinite/TiO_2 was compared with previously reported papers, as shown in Table 4.

4 Conclusions

Based on the above results, a possible mechanism to explain the improvement of photocatalytic properties of clay/TiO_2 nanocomposites was proposed. Kaolinite and halloysite are both natural clays that exhibit interesting adsorption properties. By combining these two materials, they benefit from their complementary properties for more efficient adsorption. The

Table 4: Photodegradation efficiency of Kaolinite/TiO_2 nanocomposites for different dyes.

Nanocomposite	Organic pollutant	Catalyst amount (g/L)	C_o (mg/L)	Degradation rate (%)	Reaction time	Reference
Kaolinite/TiO_2	Methyl orange	1	10	45	7 h	[68]
Kaolinite/TiO_2	Congo-red (CR)	1	20	60	4 h	[69]
Kaolinite/Ag–TiO_2	Methylene blue	0.5	3.198	96.7	120 min	[70]
Kaolinite/TiO_2	Methylene blue	0.25	10	94	5 h	[71]
Kaolinite/TiO_2	Rhodamine B	0.5	50	51	120 min	[72]
Halloysite/TiO_2	Methylene blue	0.5	30	81.6	4H	[73]
Halloysite- Carbon-TiO_2	Methylene blue	0.2	20	73	80 min	[74]
kaolinite/TiO_2	Methylene blue	1	20	98.3	3h	**This study**

grinding treatment rate over time was adequate to increase the amount of micropores and mesopores. Crystalline phase development was evaluated using X-ray diffraction data to confirm a kaolinite crystalline phase in clay and that the anatase phase only exists in kaolinite/TiO_2 composites. The photocatalytic activity of the produced nanoparticles for MB removal was investigated using a 365 nm UV light source. This study clearly shows that coating TiO_2 with Kaolinite increased the removal of MB dye. Increasing grinding time of 8 h and calcination at 600 °C also caused structural rearrangement of crystalline layers of kaolinite. At this temperature, kaolinite underwent a transformation into metakaolinite, an amorphous alumino-silicate phase. This structural rearrangement can reduce the specific surface area due to the disruption of the kaolinite sheet crystal structure.

Research ethics: Not applicable.
Informed consent: Not applicable.
Author contributions: Conceptualization, K.F., L.M., A.I., B.N. and R.B; methodology, K.F., A.S., and N.B.; validation, L.M., and A.A.; formal analysis, M.A , S.S., Q.E., K.M and A.S, investigation, K.F ; resources, S.S., A.A., and B.N.; data curation, S.A., R.B., B.N, and K.F.; writing – original draft preparation, K.F; L.M.; writing – review and editing, K.F., B.J, L.M., T.N and A.A.; visualization, K.F., I.A.; B.J, L.M., T.N and A.A supervision, B.J, L.M., T.N and A.A project administration, K.F.,I.A.; B.J, L.M., T.N and A.A All authors have read and agreed to the published version of the manuscript.
Use of Large Language Models, AI and Machine Learning Tools: None declared.
Conflict of interest: The author states no conflict of interest.
Research funding: None declared.
Data availability: Not applicable.

References

[1] T. Islam, R. Repon, T. Islam, Z. Sarwar, and M. M. Rahman, "Impact of textile dyes on health and ecosystem: a review of structure, causes, and potential solutions," *Environ. Sci. Pollut. Res.*, vol. 30, no. 4, pp. 9207–9242, 2023.

[2] J. C. Bollinger, E. C. Lima, L. Mouni, S. Salvestrini, and H. N. Tran, "Molecular properties of methylene blue for adsorption studies: a short critical review." Manuscript under examination.

[3] A. Imessaoudene, *et al*., "Adsorption performance of zeolite for the removal of Congo red dye: factorial design experiments, kinetic, and equilibrium studies," *Separations*, vol. 10, p. 57, 2023.

[4] R. Boudraa, *et al*., "Optical and photocatalytic properties of TiO_2 – Bi_2O_3 – CuO supported on natural zeolite for removing safranin-O dye from water and wastewater," *J. Photochem. Photobiol., A: Chem.*, vol. 443, p. 114845, 2023.

[5] R. Verma, S. Pathak, A. K. Srivastava, S. Prawer, and S. Tomljenovic-hanic, "ZnO nanomaterials_ green synthesis, toxicity evaluation and new insights in biomedical applications," *J. Alloys Compd.*, vol. 876, p. 160175, 2021.

[6] L. Zehlike, A. Peters, R. H. Ellerbrock, L. Degenkolb, and S. Klitzke, "Aggregation of TiO_2 and Ag nanoparticles in soil solution – effects of primary nanoparticle size and dissolved organic matter characteristics," *Sci. Total Environ.*, vol. 688, pp. 288–298, 2019.

[7] A. Mishra, A. Mehta, and S. Basu, "Clay supported TiO_2 nanoparticles for photocatalytic degradation of environmental pollutants : a review," *Environ. Chem. Eng.*, vol. 6, no. 5, pp. 6088–6107, 2018.

[8] W. Ao, *et al*., "TiO_2/Activated carbon synthesized by microwave-assisted heating for tetracycline photodegradation," *Environ. Res.*, vol. 214, p. 113837, 2022.

[9] S. Cheikh, *et al*., "Complete elimination of the ciprofloxacin antibiotic from water by the combination of adsorption–photocatalysis process using natural hydroxyapatite and TiO_2," *Catalysts*, vol. 13, 2023, https://doi.org/10.3390/catal13020336.

[10] T. Matsuura, M. A. Rahman, Z. Harun, J. Jaafar, and M. Nomura, "Fabrications and applications of low cost ceramic membrane from kaolin: a comprehensive review," *Ceram. Int.*, vol. 44, no. 5, pp. 4538–4560, 2017.

[11] L. Mouni, *et al*., "Removal of methylene blue from aqueous solutions by adsorption on kaolin: kinetic and equilibrium studies," *Appl. Clay Sci.*, vol. 153, pp. 38–45, 2018.

[12] A. Awasthi, P. Jadhao, and K. Kumari, "Clay nano – adsorbent: structures, applications and mechanism for water treatment," *SN Appl. Sci.*, vol. 1, pp. 1–21, 2019,.

[13] X. Zhu, C. Yan, and J. Chen, "Application of urea-intercalated kaolinite for paper coating," *Appl. Clay Sci.*, vol. 55, pp. 114–119, 2012.

[14] L. Junior, *et al*., "Case studies in construction materials influence of processing parameters variation on the development of geopolymeric ceramic blocks with calcined kaolinite clay," *J. Case Stud. Constr. Mater.*, vol. 16, 2022. https://doi.org/10.1016/j.cscm.2022.e00897.

[15] K. A. Buyondo, H. Kasedde, and J. B. Kirabira, "A comprehensive review on kaolin as pigment for paint and coating: recent trends of chemical-based paints, their environmental impacts and regulation," *Case Stud. Chem. Environ. Eng.*, vol. 6, p. 100244, 2022.

[16] L. Abu-Ennab, M. K. Dixit, B. Birgisson, and P. Pradeep Kumar, "Comparative life cycle assessment of large-scale 3D printing utilizing kaolinite-based calcium sulfoaluminate cement concrete and conventional construction," *Clean. Environ. Syst.*, vol. 5, p. 100078, 2022.

[17] P. Joshi, A. Raturi, M. Srivastava, and O. P. Khatri, "Graphene oxide, kaolinite clay and PVA-derived nanocomposite aerogel as a regenerative adsorbent for wastewater treatment applications," *J. Environ. Chem. Eng.*, vol. 10, no. 6, p. 108597, 2022.

[18] C. Li, *et al*., "Tuning and controlling photocatalytic performance of TiO 2/kaolinite composite towards ciprofloxacin: role of 0D/2D structural assembly," *Adv. Powder Technol.*, vol. 31, no. 3, pp. 1–12, 2020.

[19] K. Sakurai, Y. Ohdate, and K. Kazutake, "Comparison of salt titration and potentiometric titration methods for the determination of zero point of charge (ZPC)," *Soil Sci. Plant Nutr.*, vol. 34, no. 2, pp. 37–41, 2012.

[20] J. P. Simonin, "On the comparison of pseudo-first order and pseudo-second order rate laws in the modeling of adsorption kinetics," *Chem. Eng. J.*, vol. 300, pp. 254–263, 2016.

[21] N. T. Hoang, A. T. Tran, T. Le, and D. D. Nguyen, "Journal of environmental chemical engineering enhancing efficiency and photocatalytic activity of TiO 2 -SiO 2 by combination of glycerol for MO degradation in continuous reactor under solar irradiation," *J. Environ. Chem. Eng.*, vol. 9, no. 5, p. 105789, 2021.

[22] N. Bouzidi, "Study of the microstructure and mechanical properties of halloysite – kaolinite/$BaCO_3$ ceramic composites," *J. Sediment. Geol.*, vol. 53, no. 3, pp. 403–412, 2018.
[23] C. Renac and F. Assassi, "Formation of non-expandable 7 Å halloysite during eocene – miocene continental weathering at Djebel Debbagh, Algeria : a geochemical and stable-isotope study," *Sediment. Geol.*, vol. 217, no. 1–4, pp. 140–153, 2009.
[24] P. J. Sa, C. Jime, D. Haro, L. A. Pe, I. Varona, and L. Pe, "Effects of dry grinding on the structural changes of kaolinite powders,"vol. 57, pp. 1649–1657, 2000.
[25] K. Bouguermouh, N. Bouzidi, L. Mahtout, L. Pérez-villarejo, and M. L. Martínez-cartas, "Effect of acid attack on microstructure and composition of metakaolin-based geopolymers: the role of alkaline activator," *J. Non-Cryst. Solids*, vol. 463, pp. 128–137, 2017,.
[26] T. Pushpamalini, M. Keerthana, R. Sangavi, A. Nagaraj, and P. Kamaraj, "Comparative analysis of green synthesis of TiO 2 nanoparticles using four different leaf extract," *Mater. Today: Proc.*, vol. 40, pp. S180–S184, 2021.
[27] A. Mishra, A. Mehta, and S. Basu, "Clay supported TiO_2 nanoparticles for photocatalytic degradation of environmental pollutants: a review," *J. Environ. Chem. Eng.*, vol. 6, no. 5, pp. 6088–6107, 2018.
[28] A. Mishra, A. Mehta, M. Sharma, and S. Basu, "Enhanced heterogeneous photodegradation of VOC and dye using microwave synthesized TiO2/clay nanocomposites: a comparison study of different type of clays," *J. Alloys Compd.*, vol. 694, pp. 574–580, 2017.
[29] R. Chen, *et al.*, "Enhanced photocatalytic activity of kaolinite-TiO_2-graphene oxide composite with a porous stacking structure," *J. Alloys Compd.*, vol. 889, p. 161682, 2022.
[30] C. Li, Z. Sun, A. Song, X. Dong, S. Zheng, and D. Dionysiou, "Flowing nitrogen atmosphere induced rich oxygen vacancies overspread the surface of TiO_2/kaolinite composite for enhanced photocatalytic activity within broad radiation spectrum," *Appl. Catal. B: Environ.*, vol. 236, pp. 76–87, 2018.
[31] A. B. Aritonang, E. Pratiwi, W. Warsidah, S. I. Nurdiansyah, and R. Risko, "Fe-doped TiO_2/kaolinite as an antibacterial photocatalyst under visible light irradiation," *Bull. Chem. React. Eng. Catal.*, vol. 16, pp. 293–301, 2021.
[32] C. Rafael, *et al.*, "Synthesis of superacid sulfated TiO 2 prepared by sol-gel method and its use as a titania precursor in obtaining a kaolinite/TiO 2 nano-hybrid composite," *J. Powder Technol.*, vol. 381, pp. 366–380, 2021.
[33] A. L. Patterson, "The scherrer formula for X-ray particle size determination," *Phys. Rev.*, vol. 56, p. 978, 1939.
[34] X. Li, K. Peng, H. Chen, and Z. Wang, "TiO_2 nanoparticles assembled on kaolinites with different morphologies for efficient photocatalytic performance," *Sci. Rep.*, vol. 8, pp. 1–12, 2018.
[35] L. Andrini, R. M. Toja, M. S. Conconi, F. G. Requejo, and N. M. Rendtorff, "Halloysite nanotube and its firing products: structural characterization of halloysite, metahalloysite, spinel type silicoaluminate and mullite," *J. Electron Spectrosc. Relat. Phenom.*, vol. 234, pp. 19–26, 2019.
[36] H. Bel Hadjltaief, M. E. Galvez, M. Ben Zina, and P. Da Costa, "TiO_2/clay as a heterogeneous catalyst in photocatalytic/photochemical oxidation of anionic reactive blue 19," *Arab. J. Chem.*, vol. 12, no. 7, pp. 1454–1462, 2019.
[37] M. Reli, K. Kočí, V. Matejka, P. Kovář, and L. Obalová, "Effect of calcination temperature and calcination time on the kaolinite/TIO_2 composite for photocatalytic reduction of CO_2," *GeoSci. Eng.*, vol. 4, pp. 10–22, 2016.
[38] S. O. Azeez, I. O. Saheed, F. Adekola, and S. S. Shina, "Preparation of TiO_2 activated kaolinite composite for photodegradation of rhodamine B dye," *Bull. Chem. Soc. Ethiop.*, vol. 36, no. 1, pp. 13–24, 2022.
[39] J. da S. Lopes, *et al.*, "Modification of kaolinite from pará/Brazil region applied in the anionic dye photocatalytic discoloration," *Appl. Clay Sci.*, vol. 168, pp. 295–303, 2019.
[40] A. Aritonang, "Fe-doped TiO_2/kaolinite as an antibacterial photocatalyst under visible light Fe-doped TiO_2/kaolinite as an antibacterial photocatalyst under visible light irradiation," *Bull. Chem. React. Eng.*, vol. 16, pp. 293–301, 2021.
[41] G. N. Shao, M. Engole, S. M. Imran, S. J. Jeon, and H. T. Kim, "Sol-gel synthesis of photoactive kaolinite-titania: effect of the preparation method and their photocatalytic properties," *Appl. Surf. Sci.*, vol. 331, pp. 98–107, 2015.
[42] L. Vietro, *et al.*, "Kaolinite-titanium oxide nanocomposites prepared via sol-gel as heterogeneous photocatalysts for dyes degradation," *J. Catal. Today*, vol. 246, pp. 1–10, 2014.
[43] K. Mamulová Kutláková, *et al.*, "Preparation and characterization of photoactive composite kaolinite/TiO_2," *J. Hazard. Mater.*, vol. 188, no. 1–3, pp. 212–220, 2011.
[44] P. A. Fufa, *et al.*, "Visible light-driven photocatalytic activity of Cu2O/ZnO/Kaolinite-Based composite catalyst for the degradation of organic pollutant," *Nanotechnology*, vol. 33, p. 315601, 2022.
[45] M.-S. Yacoub Elhadj and X. Perrin, "Influencing parameters of mechanochemical intercalation of kaolinite with urea," *Appl. Clay Sci.*, vol. 213, p. 106250, 2021.
[46] U. O. Bhagwat, J. M. Wu, A. M. Asiri, and S. Anandan, "Sonochemical synthesis of Mg-TiO2 nanoparticles for persistent Congo red dye degradation," *J. Photochem. Photobiol. A: Chem.*, vol. 346, pp. 559–569, 2017.
[47] R. A. Maryam and J. Masoud, "Improved photocatalytic degradation of methylene blue under visible light using acrylic nanocomposite contained silane grafted nano TiO_2," *J. Photochem. Photobiol. A: Chem.*, vol. 443, 2023, https://doi.org/10.1016/j.jphotochem.2023.114832.
[48] P. Chawla, S. K. Sharma, and A. P. Toor, "Techno-economic evaluation of anatase and P25 TiO2 for treatment basic yellow 28 dye solution through heterogeneous photocatalysis," *Environ. Dev. Sustain.*, vol. 22, pp. 231–249, 2020.
[49] D. Papoulis, *et al.*, "Palygorskite- and halloysite-TiO_2 nanocomposites: synthesis and photocatalytic activity," *Appl. Clay Sci.*, vol. 50, no. 1, pp. 118–124, 2010.
[50] C. G. Joseph, Y. H. Taufiq-Yap, E. Letshmanan, and V. Vijayan, "Heterogeneous photocatalytic chlorination of methylene blue using a newly synthesized TiO2-SiO2 photocatalyst," *Catalysts*, vol. 12, no. 2, p. 156, 2022.
[51] E. D. Revellame, D. Lord, W. Sharp, R. Hernandez, and M. E. Zappi, "Adsorption kinetic modeling using pseudo- fi rst order and pseudo-second order rate laws: a review," *Clean. Eng. Technol.*, vol. 1, p. 100032, 2020,.
[52] C. Hieu, H. Nguyen, C. Fu, Y. Lu, and R. Juang, "Roles of adsorption and photocatalysis in removing organic pollutants from water by activated carbon À supported titania composites: kinetic aspects," *J. Taiwan Inst. Chem. Eng.*, vol. 109, pp. 51–61, 2020,.
[53] S. Salvestrini, "A modification of the Langmuir rate equation for diffusion-controlled adsorption kinetics," *React. Kinet. Mech. Catal.*, vol. 128, pp. 571–586, 2019.
[54] H. N. Tran, *et al.*, "Innovative spherical biochar for pharmaceutical removal from water: insight into adsorption mechanism," *J. Hazard. Mater.*, vol. 394, p. 122255, 2020.
[55] N. Mundkur, A. S. Khan, M. I. Khamis, T. H. Ibrahim, and P. Nancarrow, "Synthesis and characterization of clay-based adsorbents modified

with alginate, surfactants, and nanoparticles for methylene blue removal," *Environ. Nanotechnol. Monit. Manag.*, vol. 17, p. 100644, 2022,.

[56] A. V. Ferreira, *et al*., "Titania-triethanolamine-kaolinite nanocomposites as adsorbents and photocatalysts of herbicides," *J. Photochem. Photobiol. A: Chem.*, vol. 419, 2021, https://doi.org/10.1016/j.jphotochem.2021.113483.

[57] N. G. Asenjo, R. Santamaría, C. Blanco, M. Granda, P. Álvarez, and R. Menéndez, "Correct use of the Langmuir-hinshelwood equation for proving the absence of a synergy effect in the photocatalytic degradation of phenol on a suspended mixture of Titania and activated carbon," *Carbon*, vol. 55, pp. 62–69, 2013.

[58] H. Selpiana, A. B. Aritonang, M. A. Wibowo, W. Warsidah, and A. Adhitiawarman, "Photocatalytic dDegradation of mMethylene bBlue uUsing Fe_2O_3-TiO_2/kKaolinite under vVisible lLight iIllumination," *Kimia Dan Pendidikan Kimia*, vol. 7, no. 3, pp. 277–286, 2022.

[59] Y. Zhang, Y. Guo, G. Zhang, and Y. Gao, "Stable TiO_2/rectorite: preparation, characterization and photocatalytic activity," *Appl. Clay Sci.*, vol. 51, no. 3, pp. 335–340, 2011.

[60] E. Gaidoumi, A. Kherbeche, A. Arrahli, A. Loqman, F. Baragh, and B. El Bali, "Abdelali efficient sol-gel nanocomposite TiO 2 -clay in photodegradation of phenol: comparison to labe-made and commercial photocatalysts," *Springer Nature*, vol. 14, pp. 5401–5414, 2021,.

[61] D. Ghosh and K. G. Bhattacharyya, "Adsorption of methylene blue on kaolinite," *Appl. Clay Sci.*, vol. 20, pp. 295–300, 2001.

[62] D. Wu, *et al*., "Improved photoelectric performance via fabricated heterojunction G-C 3N4/TiO_2/HNTs loaded photocatalysts for photodegradation of ciprofloxacin," *J. Ind. Eng. Chem.*, vol. 64, no. 25, pp. 206–218, 2018.

[63] C. Li, Z. Sun, W. Zhang, C. Yu, and S. Zheng, "Highly efficient G-C3N4/TiO_2/kaolinite composite with novel three-dimensional structure and enhanced visible light responding ability towards ciprofloxacin and S. Aureus," *Appl. Catal. B Environ.*, 2017, https://doi.org/10.1016/j.apcatb.2017.08.044.

[64] B. Zhao, L. Liu, and H. Cheng, "Rational design of kaolinite-based photocatalytic materials for environment decontamination," *Appl. Clay Sci.*, vol. 208, p. 106098, 2021.

[65] X. Hu, *et al*., "Mechanisms underlying the photocatalytic degradation pathway of ciprofloxacin with heterogeneous TiO_2 xi," vol. 380, pp. 122366, 2020.

[66] A. A. Isari, A. Payan, M. Fattahi, S. Jorfi, and B. Kakavandi, "Photocatalytic degradation of rhodamine B and real textile wastewater using Fe-doped TiO2 anchored on reduced graphene oxide (Fe-TiO2/RGO): characterization and feasibility, mechanism and pathway studies," *Appl. Surf. Sci.*, vol. 462, pp. 549–564, 2018.

[67] C. Yang, *et al*., "Highly-efficient photocatalytic degradation of methylene blue by PoPD-modified TiO_2 nanocomposites due to effect of TiO_2 with PoPD," *J. Sci. Rep.*, vol. 7, p. 3973, 2017.

[68] C. Wang, H. Shi, P. Zhang, and Y. Li, "Applied clay science synthesis and characterization of kaolinite/TiO 2 nano-photocatalysts," *Appl. Clay Sci.*, vol. 53, no. 4, pp. 646–649, 2011.

[69] M. Alkhabbas, F. Odeh, K. Alzughoul, R. Afaneh, and W. Alahmad, "Jordanian kaolinite with TiO 2 for improving solar light harvesting used in dye removal," *MDPI*, vol. 28, no. 3, p. 989, 2023.

[70] S. Sudeshna, D. Arundhuti, and B. Krishna Gopal, "Photocatalytic degradation of methylene blue in aqueous solution with silver-kaolinite-titania nanocomposite under visible light irradiation," *Nanostruct*, vol. 12, no. 2, pp. 426–445, 2022.

[71] W. Hajjaji, *et al*., "Effective removal of anionic and cationic dyes by kaolinite and TiO 2/kaolinite composites," *Clay Miner.*, vol. 51, no. 1, pp. 19–27, 2016.

[72] S. O. Azeez, I. O. Saheed, F. Adekola, and S. S. Shina, "Preparation of TiO2 activated kaolinite composite for photodegradation of rhodamine B dye," *Bull. Chem. Soc. Ethiop.*, vol. 36, no. 1, pp. 13–24, 2022.

[73] Y. Du and P. Zheng, "Adsorption and photodegradation of methylene blue on TiO_2 -halloysite adsorbents," *Korean J. Chem. Eng*, vol. 31, pp. 2051–2056, 2014.

[74] L. Jiang, Y. Huang, and T. Liu, "Enhanced visible-light photocatalytic performance of electrospun carbon-doped TiO 2/halloysite nanotube hybrid nanofibers," *J. Colloid Interface Sci.*, vol. 439, pp. 62–68, 2015.

Supplementary Material: This article contains supplementary material (https://doi.org/10.1515/ijcre-2024-0145).